

# Gamma-irradiation-induced micro-structural variations in flame-retardant polyurethane foam using synchrotron X-ray micro-tomography

A. K. Agrawal,<sup>a\*</sup> B. Singh,<sup>a</sup> Y. S. Kashyap,<sup>a</sup> M. Shukla,<sup>a</sup> B. S. Manjunath<sup>b</sup> and S. C. Gadkari<sup>a</sup>

Received 24 October 2018

Accepted 8 July 2019

Edited by I. Lindau, SLAC/Stanford University, USA

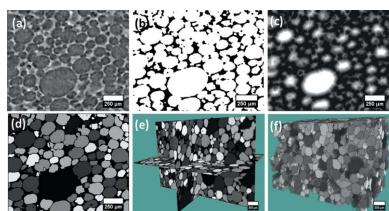
**Keywords:** X-ray imaging; micro-tomography; synchrotron imaging; polyurethane foam; gamma irradiation; morphological image analysis; cellular microstructure; structure–property relation; synchrotron X-ray micro-tomography.

<sup>a</sup>Technical Physics Division, Bhabha Atomic Research Centre, Mumbai, India, and <sup>b</sup>Reactor Technology Division, Bhabha Atomic Research Centre, Mumbai, India. \*Correspondence e-mail: ashishka@rrcat.gov.in

Flame-retardant polyurethane foams are potential packing materials for the transport casks of highly active nuclear materials for shock absorption and insulation purposes. Exposure of high doses of gamma radiation causes cross-linking and chain sectioning of macromolecules in this polymer foam, which leads to reorganization of their cellular microstructure and thereby variations in physico-mechanical properties. In this study, in-house-developed flame-retardant rigid polyurethane foam samples were exposed to gamma irradiation doses in the 0–20 kGy range and synchrotron radiation X-ray micro-computed tomography (SR- $\mu$ CT) imaging was employed for the analysis of radiation-induced morphological variations in their cellular microstructure. Qualitative and quantitative analysis of SR- $\mu$ CT images has revealed significant variations in the average cell size, shape, wall thickness, orientations and spatial anisotropy of the cellular microstructure in polyurethane foam.

## 1. Introduction

Transport casks for highly active nuclear materials such as discharged fuel pins are designed to alleviate a variety of safety hazards under different accidental conditions (Palacio, 2017; Sharma *et al.*, 2014). National and international regulations specify a series of hypothetical tests for these transportation packages, one of which is the free drop test onto an unyielding target, that mimic worst accidental scenarios (Pfeiffer & Kennedy, 1989; Sanyal *et al.*, 2011). Such applications call for impact limiters, which can mitigate the harsh environment of impact without causing appreciable stress in the packaged components (Saliba *et al.*, 2011; Diersch *et al.*, 1994; Kasperek *et al.*, 2011). These impact limiters need to be designed and optimized for their desired performance (Choi & Seo, 2010; Mane *et al.*, 2017; Kim *et al.*, 2007). Polyurethane foams (PUFs) are used as packing materials and energy absorbers in industrial applications due to their unique physico-mechanical properties such as lightweight, low thermal conductivity, low density, excellent dimensional stability, high strength-to-weight ratio, low water absorption, high crushability, good energy absorption under compression and excellent thermal insulation (Engels *et al.*, 2013; Yusuf *et al.*, 2016). These excellent properties of PUF make it a potential material for packing and impact reducer in transport packages of nuclear material. The physico-mechanical properties of PUF are strongly correlated with its density, composition and microstructure at different scales (Thirumal *et al.*, 2009, 2010; Dolomanova *et al.*, 2011; Saadatfar *et al.*, 2004). In particular, microstructure at the cellular level, characterized by shape,



size and orientation of pores, strut and wall thickness, connectivity and spatial anisotropy of pores and strut network, holds a strong correlation with its mechanical and transport properties (Banhart, 2001; Saadatfar *et al.*, 2005; Roberts & Knackstedt, 1995; Benouali *et al.*, 2005). Flame-retardant rigid PUFs used in this study are the materials specifically designed and developed for application as protective enclosures of radioactive nuclear materials in their shipping casks for safety against impact and fire during accidents. These shipping casks of radioactive materials contain a high level of radioactivity. As a result, the packing material is exposed to high doses of gamma radiation and it is desirable that the packing materials possess a certain degree of resistance to radiation or that the modifications in its physico-mechanical properties due to irradiation are at least well understood. Since exposure of gamma radiation potentially affects the compressibility and energy-absorbing capacity of polymers and variation of physico-mechanical properties are strongly correlated with the microstructure, it is important to study the gamma-irradiation-induced morphological variations in the PUF at different doses to ensure its performance during in-field application (Chen *et al.*, 2015; Mrlík & Maadeed, 2016; Bhatt *et al.*, 1999; Del Cui *et al.*, 2006).

In this study, synchrotron radiation micro-computed tomography (SR- $\mu$ CT) has been used to visualize and quantify the effects of gamma irradiation dose of several kGy on the cellular microstructure of PUF. The SR- $\mu$ CT technique is a high-resolution imaging technique that allows three-dimensional (3D) visualization and quantitative analysis of microstructure and density distribution in heterogeneous materials (Kinney & Nichols, 1992; Cnudde & Boone, 2013). The technique is best suited to porous materials where there exists a distinctive difference in attenuation coefficient between the solid and gaseous phase. In comparison with conventional  $\mu$ CT systems, SR- $\mu$ CT imaging offers a high signal-to-noise ratio, which is useful for visualization and analysis of fine features in the PUF, such as small pores and thin inter-pore walls, with improved clarity (Marenzana *et al.*, 2014). Highly collimated and intense synchrotron beam offers phase contrast enhancement at the pores edges, thereby allowing easy segmentation for quantitative structural analysis (Zhou & Brahme, 2008). Moreover, use of monochromatic beam at synchrotron imaging beamlines produces  $\mu$ CT images without any beam hardening artefacts, which is important in the segmentation of structural features and quantitative density analysis (Kaestner *et al.*, 2008). With this improved image quality, we have applied various image analysis techniques for quantitative characterization of morphological and microstructural properties such as porosity and pore size distribution, strut size distribution, connectivity and anisotropy (Moreno-Atanasio *et al.*, 2010).

## 2. Material and methods

### 2.1. Sample preparation

Samples under investigations are high-density, flame-retardant, closed-cell, rigid polyester polyol-based PUFs of density

288 kg m<sup>-3</sup> (Thirumal *et al.*, 2009, 2010). They were produced by reacting polyester polyols and isocyanate with water as a blowing agent. Polymeric methane diphenyl diisocyanate (PMDI) and sucrose-based polyether polyol were obtained from Huntsman International, Mumbai, India (Daltolac R180 and Suprasec 5005 are trademarks of Huntsman). Distilled water was used as a chemical-blowing agent. *N,N,N,N,N*-pentamethyl diethylene triamine (PMDETA) was used as a catalyst. Polyether dimethyl siloxane was used as a surfactant. All these raw materials, except PMDI, were first well mixed in a plastic beaker. Then PMDI was added into the beaker with vigorous stirring for 10 s. The amount of PMDI required for the reaction with polyether polyol and distilled water was calculated from their equivalent weights. The foam blocks were developed in well designed mould (50 × 50 × 50 mm) enclosures to achieve high density by arresting free rise. After the preparation, the foams were kept in an oven at 78°C for 24 h to complete the polymerization reaction. Different test samples of specific shapes were cut from the cured foam. Dimensional finishing was achieved through rubbing with fine emery paper. As-prepared samples were subjected to  $\gamma$  doses of 0, 5, 10, 15 and 20 kGy with air as environmental condition using a <sup>60</sup>Co-based  $\gamma$ -irradiator gamma chamber 5000 with a dose rate of 0.2 kGy h<sup>-1</sup>. Three samples of size ~4 mm × 4 mm × 10 mm were cut from different regions of each block of gamma-irradiated samples using a precision sample cutter to ensure that the cutting process did not introduce any extra damage and then used further for SR- $\mu$ CT-based micro-structural investigations.

### 2.2. Experimental setup

The SR- $\mu$ CT experiments were conducted on the imaging beamline BL-4 at Indus-2, a third-generation Indian synchrotron radiation source (Agrawal *et al.*, 2015; Gupta *et al.*, 2017; Fatima *et al.*, 2017; Choudhary *et al.*, 2017). The imaging beamline is installed on a 10° port of a bending-magnet source, which can be operated in monochromatic as well as white beam modes. A double-crystal monochromator, with Si (111) crystals, is used to select suitable X-ray beam within the energy range 8–35 keV with energy resolution ~10<sup>-4</sup>. The experimental station of the beamline is located at 25 m from the tangent point.

The experimental setup consists of motorized precision stages (Huber *x*, *y* and *z* translation and a rotation stage), a centrally fitted chuck for holding the samples and an X-ray imaging area detector. The X-ray detector consists of a high-resolution CCD camera with an active area of 4008 × 2672 (pixel pitch 4.5  $\mu$ m), with Gadox scintillator at its input face coupled to the CCD via a 1:2 fibre-optic taper (Photonic Science VHR-11) (Agrawal *et al.*, 2015). Fig. 1 shows a photograph of the SR- $\mu$ CT experimental setup.

### 2.3. Data acquisition

The X-ray energy and image exposure time were chosen to optimize transmission through the samples and maximize the signal-to-noise ratio in the acquired images. We have used an

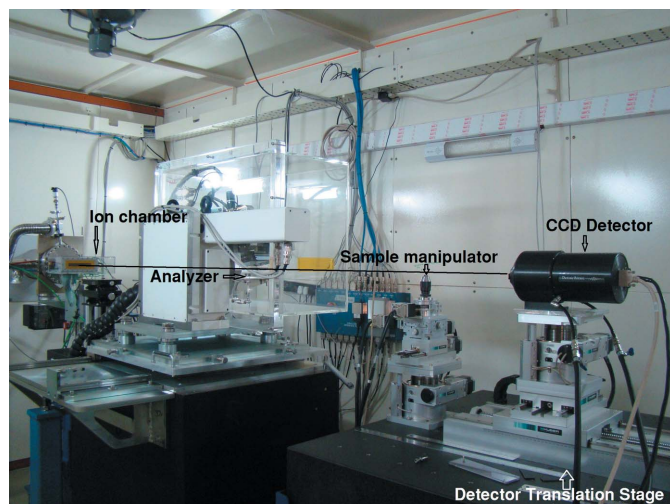


**Figure 1**  
Experimental station at imaging beamline BL-4 showing different components of the data acquisition setup.

X-ray beam energy of 10 keV (flux density  $1.8 \times 10^8$  photons  $s^{-1} \text{mm}^{-2}$ ) and an object-to-detector propagation distance of 200 mm in all our experiments. The sample was fixed on the rotation stage with a centrally fitted chuck and aligned so as to have its rotation axis perpendicular to the optical axis and parallel to a single detector column to avoid any centre of rotation error during reconstruction. The data were collected by rotating the sample about this axis through  $180^\circ$  with a rotation step of  $0.2^\circ$ , and projection images for each step were collected with an acquisition time of 800 ms. The total data acquisition time for one SR- $\mu$ CT scan was approximately 15 min including data transfer time for the snaps. In these experimental conditions, the dose delivered to the sample for a complete SR- $\mu$ CT scan was calculated to be only  $5.4 \times 10^{-5}$  Gray (Bharti *et al.*, 2016, 2017). This is much smaller than the dose value considered in this study. It is verified using optical microscopy that this small dose does not affect the PUF microstructure at the resolution scales studied here.

#### 2.4. Image reconstruction and visualization

For each sample data, the collected projection images were flat-field-corrected using reference and background images to avoid artefacts due to beam non-uniformity and detector background features. These images were further normalized to take care of the beam intensity fluctuation during data acquisition. The corrected projection images were converted into sinograms, and tomographic slice images were then reconstructed using filtered back-projection algorithms (Kak *et al.*, 2002). Tomography reconstructed cross-sectional slice images represent the local distribution of the attenuation coefficient in the sample and thus offer visualization of local micro-structural and density variations (Banhart, 2001). Representative reconstructed slice images for polyurethane samples for various irradiation doses are shown in Figs. 2(a)–2(e). The reconstructed slice images were further stacked together to make volumetric images of the samples and

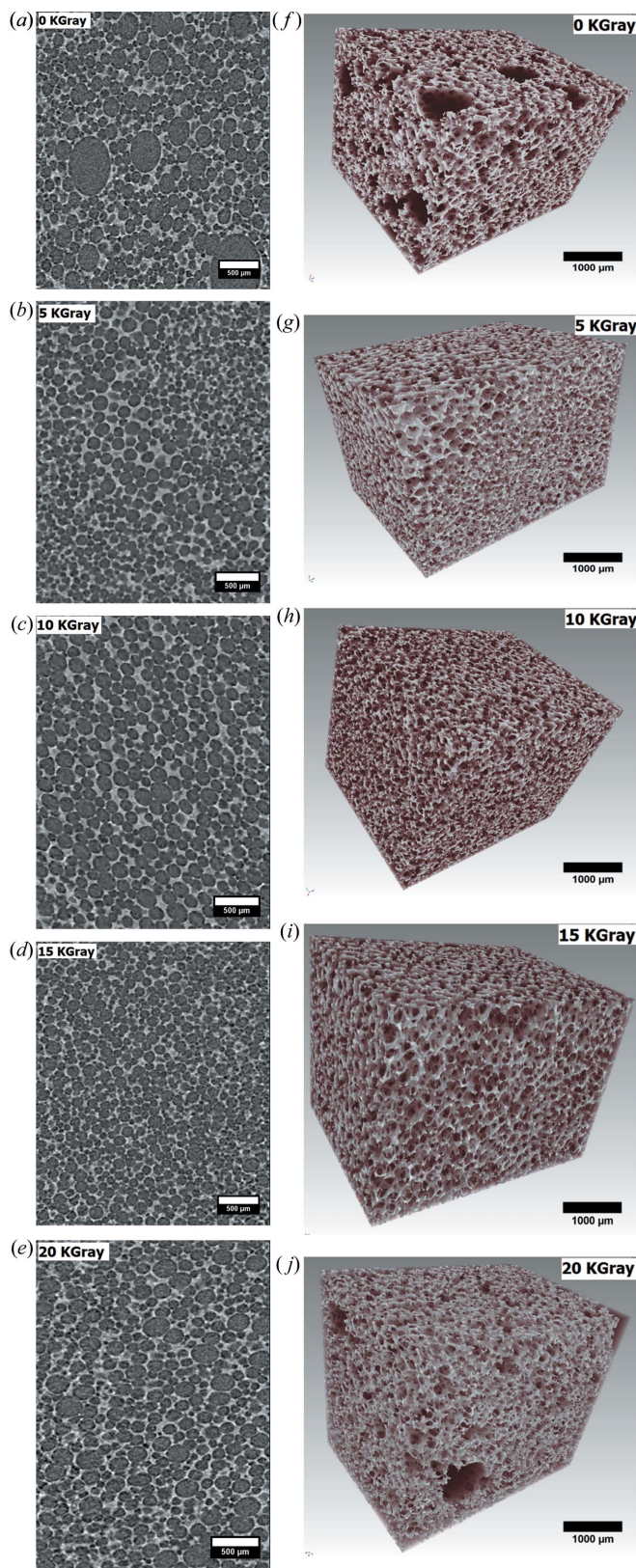


**Figure 2**  
Comparison of SR- $\mu$ CT images of PUF samples irradiated with different doses of gamma radiation. (a–e) SR- $\mu$ CT reconstructed cross-sectional slice images. The dark grey regions represent pores whereas light grey regions represent struts. (f–j) 3D volume rendered images. The images show variation of pore size, strut size, shape and uniformity of the cellular microstructure due to gamma radiation.

visualize their microstructure in three dimensions. Volume rendering was applied to remove background features and highlight sample structural details such as pores and threads to improve visibility in three dimensions as shown in Figs. 2(f)–2(j) using *ImageJ* (Limaye, 2012).

### 2.5. Image analysis

The 3D porous cellular structure of PUF can be quantified in terms of parameters such as porosity, pore and strut size distribution, pore shape, orientation, anisotropy, connectivity *etc.* These parameters were calculated by applying various morphological operations on the SR- $\mu$ CT images (Kaestner *et al.*, 2008; Moreno-Atanasio *et al.*, 2010). The segmentation and quantitative analysis on all of the samples was carried out in 3D using *ImageJ* and *Morpho+* software (Brabant *et al.*, 2011). To facilitate quantitative analysis, the reconstructed slices were first pre-processed to remove high-frequency noise present in the images through utilization of a 3D median filter followed by a bilateral filter (Sheppard *et al.*, 2004). The noise-free grey scale images thus obtained were then binarized using a threshold method to segment regions with polymer matrix and enclosed air phase in the porous region (Eliceiri *et al.*, 2012). The choice of threshold is based on the intersection of the tangent line of the respective peaks corresponding to polyurethane and air in the histogram of the complete stack of reconstructed slice images. PUF shows an open cell porous microstructure. Thus, to calculate the pore size distribution, first the boundaries of the cell need to be identified and closed using a suitable set of morphological operations. Using Euclidian distance transformation on the threshold images, distance maps of the images were obtained. Following this, watershed segmentation with suitable optimization was applied on all of the images to define the boundaries of porous cells in the polymer microstructure. To avoid over-segmentation, a region-merging algorithm was applied (Sheppard *et al.*, 2004; Doube *et al.*, 2010). After separation, various cells were labelled with their respective unique identifiers. The sequence of different morphological operations applied on the reconstructed slice images is shown in Fig. 3. Structural parameters such as equivalent diameter, maximum opening, pore surface area, shape, volume and orientation angle were then measured based on the fitting of an appropriate 3D ellipsoid within the volume of each cell. Apart from that, the connectivity and anisotropy of size/shape distribution were also measured using nearest-neighbour and maximum intercept length methods, respectively. These parameters were then compared for polyurethane samples irradiated with different doses. To ensure 3D analysis, all the operations were carried out on a complete 3D stack of reconstructed slice

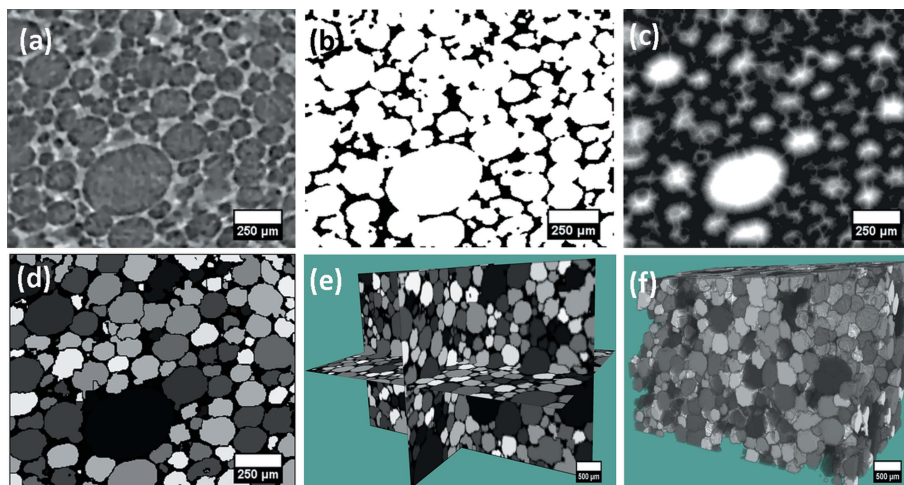


**Figure 3**

Sequence of morphological operations applied on reconstructed slice images for separation of connecting cells in porous structures. (a) Representative reconstructed slice image. (b) Threshold image. (c) Euclidian distance transformation. (d) Watershed transformation. (e–f) 3D volume images of the sample showing 3D segmented pores.

images and the filters or morphological operation applied are 3D in nature so that true 3D morphological quantities were calculated (Eliceiri *et al.*, 2012).

## 3. Results

### 3.1. Qualitative observations of SR- $\mu$ CT images

X-ray micro-tomography is a multi-informative non-destructive imaging technique. The two-dimensional grey scale cross-sectional slice images of the sample produced in X-ray micro-tomography show the local distribution of the linear attenuation coefficient of the enclosed material phases and thus allow visualization of the local micro-structure and map the density distribution at various sectional planes (Kaestner *et al.*, 2008). In order to observe the geometry and uniformity of the porous microstructure and compare them for various irradiated PUF samples, SR- $\mu$ CT reconstructed cross-sectional slice images from the central region of the reconstructed volume are shown in Fig. 2. The dark grey coloured portions in Figs. 2(a)–2(e) show the presence of pores (voids) and the light grey portions correspond to the solid phase (struts). The images depict the typical cellular microstructure of various PUF samples after exposure to different gamma radiation doses. All the samples in Fig. 2 are identified to have an open cell porous microstructure where ellipsoidal pores are bounded by a network of solid struts. The shape of the pore is well defined in all the samples; however, the size and its spatial distribution vary in different samples. It may also be noted that the percentage area of the voids is much larger than that of the struts, which indicates that samples are highly porous in nature. Qualitative comparison of these images clearly reveals the variation of cellular microstructure due to irradiation. In the un-irradiated sample, pores are found to be almost round in shape with a few exceptions. There are small as well as large

size pores; thus there exists large variations in pore sizes. The pores are interconnected but their distribution is not uniform throughout the sample. As the radiation dose increases to 5 kGy, the average cell size of the porous microstructure appears to be decreasing whereas the strut thickness appears to be increasing. This may be attributed to radiation-induced cross-linking at the macromolecular level in the polymeric chains, which is seen in the form of shrinking of the porous structure at the microscopic level (Shintani & Nakamura, 1991; Shintani *et al.*, 1991). The pores are now uniform in shape and size but spatial uniformity is still limited. This trend of cross-linking and shrinking is continued in the 10 kGy exposed sample where, apart from a decreased average pore size, an increased strut size and well defined pore shape, the spatial uniformity of the pores also appears to be improved. The whole sample contains pores of almost similar shape and size. Further enhancement of the gamma irradiation dose leads to chain scission of polymeric macromolecules, which is seen as cell rupture in slice images. This effect is observed in the form of increased cell size and decreased strut thickness, as can be seen in the slice images of the samples irradiated with 15 and 20 kGy. In these samples, pore boundaries are distorted, thus pore shape and size becomes less well defined compared with the 5–10 kGy irradiated samples. Although this analysis of cross-sectional slice images provides reasonably accurate information about microstructure and its variation due to irradiation dose, it leaves the chance of ambiguity in the results due to limitations of manual comparison on a small set of images and their two-dimensional nature. In order to support our observations and obtain a global idea of variation in cellular microstructure due to different irradiation doses, they need to be supported by 3D volume rendered images and quantitative analysis of various structural parameters. The comparison of cell morphology in the 3D volume rendered images shown in Figs. 2(f)–2(j) confirms our observations from sectional slice images and provides a rough estimate of cell morphology in terms of 3D shape, size and orientations. The pore shape is observed to be nearly ellipsoidal without any significant distortions in all the samples; however, the size of the pores and struts vary when different samples of irradiated PUFs are compared.

### 3.2. Quantitative 3D image analysis

Inspection of 2D and 3D micro-CT images provides sufficient qualitative understanding of PUF microstructure and its variation due to gamma irradiation. However, in order to obtain accurate measurements of structural parameters and their comparison for various samples, quantitative analysis of the tomography data has also been carried out (Kaestner *et al.*, 2008; Moreno-Atanasio *et al.*, 2010; Sheppard *et al.*, 2004; Doube *et al.*, 2010; Eliceiri *et al.*, 2012). This analysis allows quantitative values of irradiation dose induced variations in porosity, density, morphology, pore and strut size, shape, orientation, connectivity and anisotropy for various irradiated PUF samples. The 3D quantitative analysis is also useful in establishing relations between micro-structural and physico-

mechanical properties using semi-empirical models or finite-element modelling.

**3.2.1. Porosity and its spatial inhomogeneity.** As seen in the qualitative analysis, irradiation of PUF with gamma dose affects its overall porosity. Measurement of the porosity was carried out in terms of volume fractions, *i.e.* the ratio of solid and porous volumes out of the total tomographic reconstructed volumes of the samples (Doube *et al.*, 2010; Eliceiri *et al.*, 2012). A comparison of the solid and pore fraction along with porosity for various PUF samples irradiated with different doses is given in Table 2 later. The porosity tends to decrease initially with irradiation doses up to 10 kGy, but is further increased if the irradiation dose is increased to 15 and 20 kGy. It is also seen in qualitative analysis that the distribution of porosity is not homogeneous for some of the samples, thus we have measured the spatial variation of the porosity within the tomography imaged volume. The 3D volume data were sequentially eroded from the outermost layers of all sides in the inward direction and the porosity was calculated for the remaining 3D volume of the samples. The spatial variation of the porosity is shown in Fig. 4(a) for various polyurethane samples. These results show that there are local variations of porosity in the range 2–5% in all the samples except the sample irradiated with 20 kGy; for the sample 20 kGy-irradiated sample, inward porosity shows a systematic increment towards the core, suggesting that the inner region is more porous than the outer region. Close observation of this sample shows that it contains an exceptionally large-size pore in the central region causing highly increased porosity towards the core.

**3.2.2. Density and its spatial inhomogeneity.** The voxel grey values in SR- $\mu$ CT images are directly proportional to the local X-ray attenuation coefficient of the sample averaged over the volume of the voxel, which further depends on its atomic composition and density. In a two-phase porous material like PUF, the solid material is distributed only in the strut region connecting the pores and these struts are seen with higher grey values compared with the pores. The ‘averaged grey value’ of a region defined as the statistical mean of the grey values of all voxels in the selected region is also affected by its porosity; therefore, it is also proportional to the physical density of the sample. In our case, we have measured the average grey values of various samples of gamma-irradiated samples and its local spatial variations within the respective samples to compare the variation of their physical density and its homogeneity. The results given in Table 1 and Fig. 4(b) indicate that the density increases initially with irradiation dose up to 10 kGy due to cross-linking induced shrinking and densification but decreases when the irradiation dose is increased beyond 10 kGy causing chain scission. The spatial inhomogeneity of density in the PUF samples due to gamma irradiation dose is also calculated in terms of variation of averaged grey values and is shown in Fig. 4(b). The method applied for this calculation is similar to the method adopted for calculation of inhomogeneity of porosity. These results show that there is only a 2–3% variation in spatial distribution of the average grey values for all the samples except for the

**Table 1**

Quantitative parameters related to size, shape, orientation and density (quantities in brackets show the standard deviation).

	0 kGy	5 kGy	10 kGy	15 kGy	20 kGy
Equivalent diameter ( $\mu\text{m}$ )	88.40 (38.53)	81.5628 (28.36)	80.798 (34.65)	85.2742 (32.72)	106.572 (28.23)
Maximum opening ( $\mu\text{m}$ )	123.01 (47.11)	117.12 (34.16)	111.65 (32.46)	115.63 (41.5251)	147.65 (44.34)
Strut size ( $\mu\text{m}$ )	30.00 (9.12)	32.70 (10.11)	37.66 (8.30)	34.07 (9.80)	33.28 (11.51)
Sphericity	0.715 (0.063)	0.710 (0.059)	0.698 (0.064)	0.718 (0.075)	0.720 (0.089)
Plateness of struts	<i>b/a</i>	0.62	0.62	0.613	0.626
	<i>c/a</i>	0.368	0.368	0.382	0.378
Orientation ( $\theta$ )	102.978 (64.62)	86.7811 (29.46)	95.6913 (26.88)	75.9952 (35.87)	88.4658 (42.26)
Orientation ( $\phi$ )	1.34411 (53.40)	33.1284 (50.18)	10.1002 (72.15)	14.4694 (57.74)	3.18078 (60.53)
Average grey value	97.9127 (32.8703)	100.816 (34.9542)	100.815 (32.8703)	99.7421 (34.0623)	95.3431 (32.2344)

20 kGy sample, thus the results indicate that the effect on density is nearly uniform throughout the samples for all of the samples. The sharp variation in the average grey value of the 20 kGy sample towards the core is due to the presence of one exceptionally large pore causing relatively higher porosity in the core for this sample (Doube *et al.*, 2010).

**3.2.3. Pore and strut size distribution.** Several physical properties of porous materials such as compressibility, permeability, toughness *etc.* depend on the size distribution of the pores and struts (Kenesei *et al.*, 2004; Jang *et al.*, 2008). A detailed 3D investigation of pores in  $\mu\text{CT}$  images gives accurate estimates of pore and strut size, shape and orientation, which can be used in various empirical models for calculating different mechanical and transport properties (Saadatfar *et al.*, 2005; Roberts & Knackstedt, 1995).

The pore diameters and strut thicknesses were measured using a method generally adopted in the analysis of trabecular bone structures (Doube *et al.*, 2010). In this method, the thickness measured is the diameter of the greatest sphere that fits within the structure. Depending on the choice of foreground pixels in the binary image, the size of the pores or struts can be measured using the same procedure in terms of pore diameter and strut thickness, respectively. Two-dimensional colour-coded maps of pore diameter and strut thickness are shown in Figs. 5(a)–5(e) and 5(f)–5(j), respectively, to show their spatial distribution within the sample. The colour of a pore or strut represents its size as per the colour bars shown in the images. Exclusive analysis of  $\mu\text{CT}$  images has also been carried out for measuring the statistical distribution of pore sizes. In closed cell foams, this is relatively easy by adopting methods similar to locating inclusions in particulate composites; however, estimation of pore size is not possible by the inclusion method for open cell porous structure in our PUF samples. For measuring pore size in such an interconnected network, specific image analysis procedures need to be followed in which the connected pores are first systematically separated into individual pores using pore identification and separation algorithms as discussed in the previous section. The size of the pores was measured in terms of the maximum opening, which is the length of the largest accommodating straight line within the cell (Eliceiri *et al.*, 2012). Pore volume was measured in terms of equivalent diameter, which is the diameter of a sphere with an equivalent volume to that of the pore/cell (Sheppard *et al.*, 2004). To study the pore size variation due to gamma irradiation, the mean values with standard deviations of both these measurements are tabulated in Table 1. Fig. 6(a) shows the frequency distribution of equivalent diameter of pores for polyurethane foam samples irradiated with different gamma dose. It can be seen from both of these measurements that the mean equivalent diameter and maximum opening of the PUFs decreases initially with

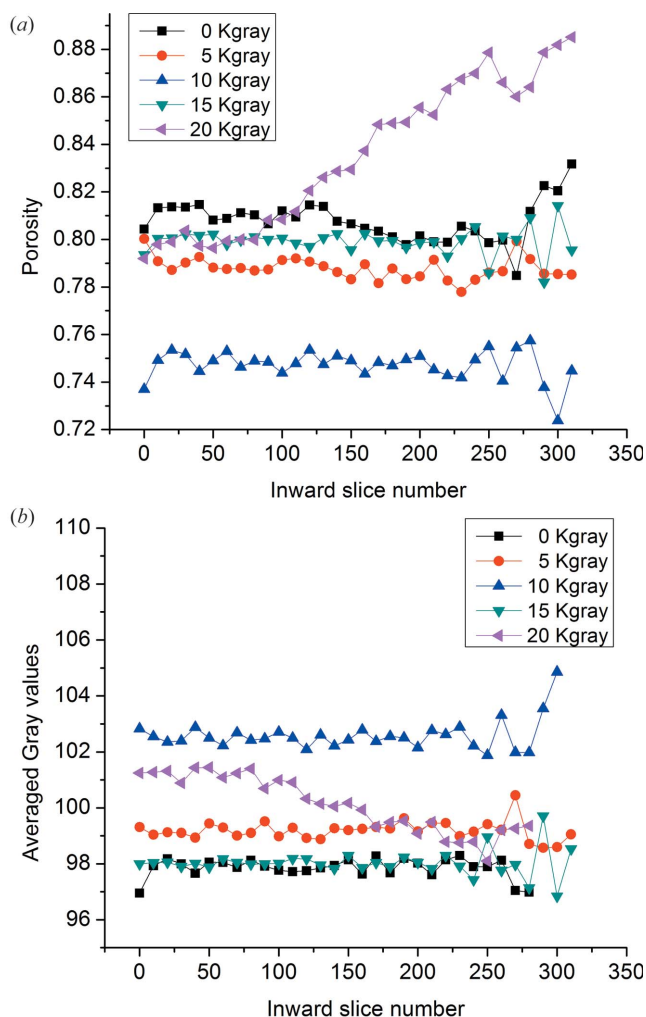


**Figure 4** Measurement of inward homogeneity in the porous microstructure of PUF samples with different doses of gamma radiation. A skin of thickness equal to 10 pixels was removed from all directions in the reconstructed volume, and porosity and average grey value were calculated for the remaining volume. (a) Inward porosity variation. (b) Inward average grey value variation.

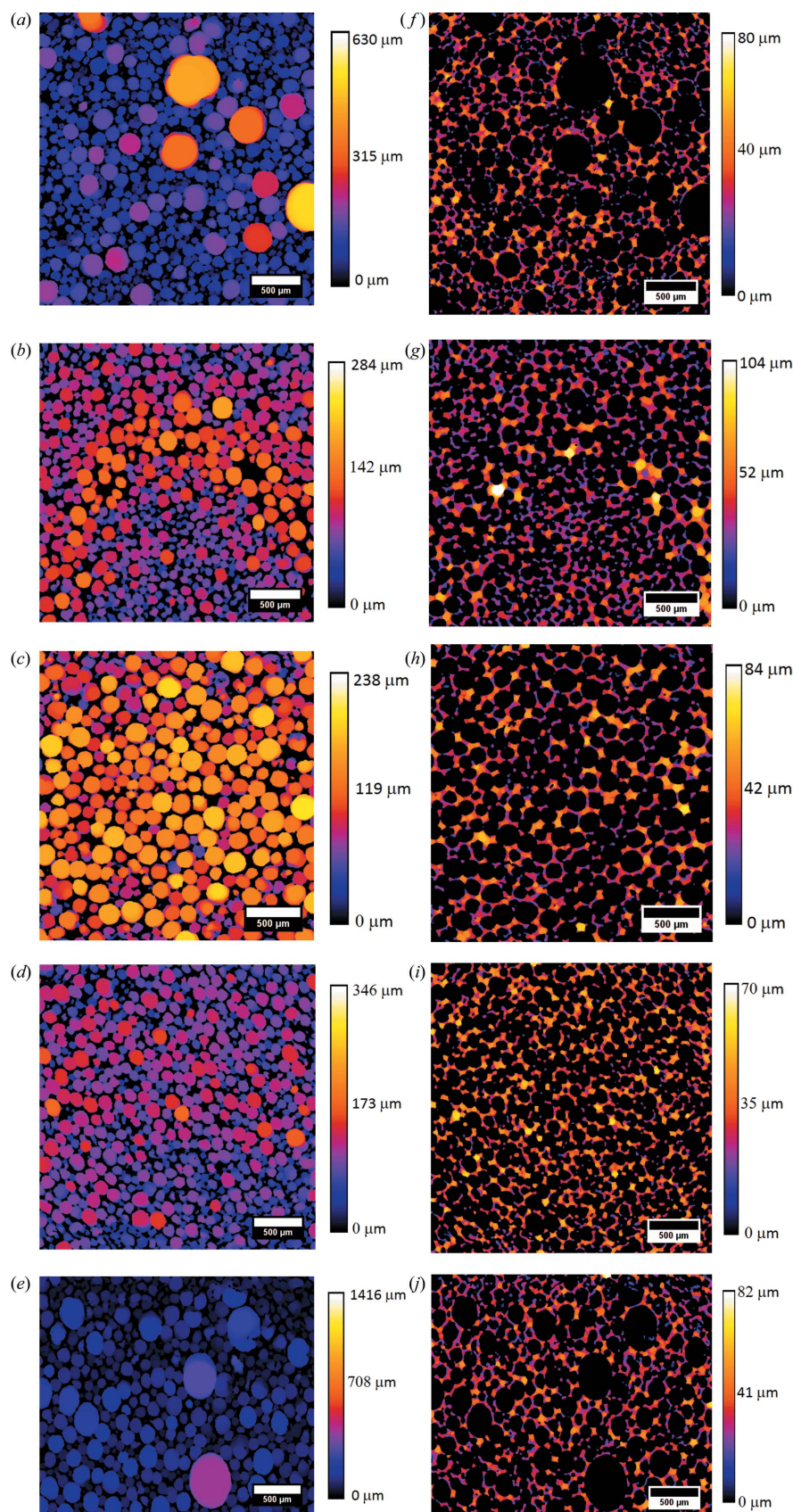


**Figure 5**  
Thickness maps of pores (a–e) and struts (f–j) in the PUF samples treated with different doses of gamma radiation. The colour code in the images represents the diameter of pores or thickness of struts as per the colour bar included in the image.

increased irradiation dose up to 10 kGy, but increases further up to some extent when the samples are irradiated with higher doses. The mean values of the maximum opening are comparatively larger compared with the equivalent diameter, which is a direct consequence of their definitions. Since pores are not perfect spheres, the length of the maximum accommodating line would be larger compared with the radius of a sphere with equivalent volume for all the pores. This behaviour is in quite good agreement with the qualitative visualization of the SR- $\mu$ CT reconstructed cross-sectional slice and 3D images.

**3.2.4. Pore and strut shape.** Mechanical and transport properties of porous polymers are greatly influenced by the shape and orientation of the pores present (Benouali *et al.*, 2005). For example, higher sphericity leads to improved toughness in the bio-ceramic (Veljović *et al.*, 2011). Permeability has also been reported to have a dependence of pore shape and orientation (Seuba *et al.*, 2016). Similarly, variation in sphericity of pores also affects piezoelectric and dielectric properties of materials (Zeng *et al.*, 2007). In cases of porous polyurethane, open pores are large which can provide high compressibility and permeability. Thus, it is necessary to study the sphericity and orientation of pores present in PUFs irradiated with different doses. It is observed that in the qualitative analysis of all images of Figs. 3(a)–3(j) that the pores are spheroid; however, the size and sphericity varies. Further, in quantitative analysis, the shape of the pores was measured in terms of sphericity and its histogram distribution for various samples as shown in Fig. 6(b). The sphericity is a measure of the deviation of shape from a perfect sphere and finds its value between zero and one (Sheppard *et al.*, 2004). It can be seen that the sphericity of the majority of pores for all of the samples lies between 0.5 and 0.8, thus most of the pores are ellipsoidal in shape, elongated or compressed in one direction. Mean values and standard deviations of various measurements are also included for comparison in Table 1. A comparison of these data shows that the sphericity does not vary much with irradiation dose and remains nearly equal to 0.7 for all cases.

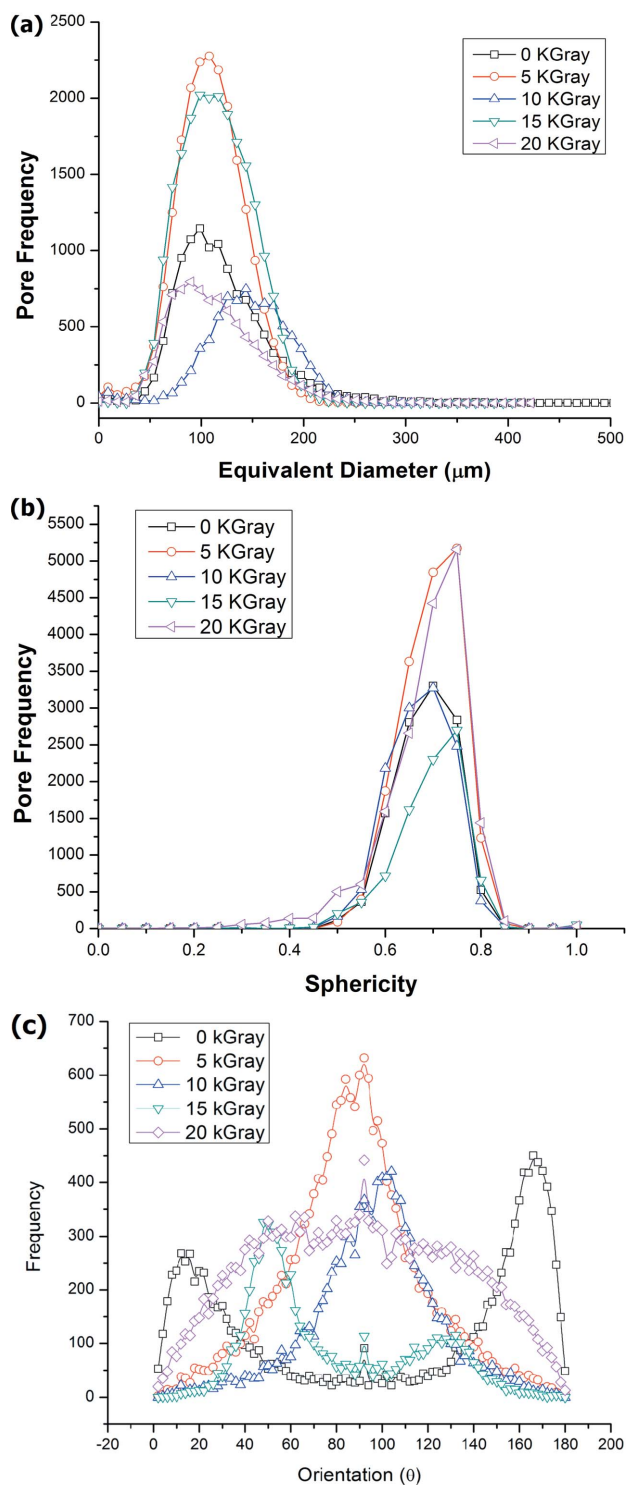


**Figure 6** Histogram distribution of the microstructural properties of PUF irradiated with different gamma doses. (a) Equivalent diameter. (b) Sphericity. (c) Orientation angle.

The shape of the struts was measured in terms of plateness. In calculating the plateness, first the 3D structure is skeletonized to obtain the medial axis of the strut, which is used as the seed for sampling. Random vectors are seeded from each voxel on the medial axis until every vector has hit a foreground–

background boundary. For each seed voxel, a covariance matrix is constructed from the vectors times their lengths. Eigen value decomposition results in an ordered list of three axis lengths. The three lengths are summed over all seed points to give  $\sum a$ ,  $\sum b$  and  $\sum c$ , from which the relative proportions of rod- and plate-like structures may be inferred. Rod-like structures have a single long axis ( $a$ ) and two short axes ( $b, c$ ) such that  $a \gg b > c$ , whereas disc-shaped, plate-shaped structures have two longer axes ( $a, b$ ) and one much shorter axis ( $c$ ) so that  $a > b \gg c$ . It can be seen that the struts are rod-like shaped for all samples and their plateness does not change much due to gamma irradiation of different doses. The measured plateness values are given in Table 2 for various irradiated samples.

**3.2.5. Pore orientation.** The orientation of non-spherical pores also affects the mechanical and transport properties of porous materials (Chen *et al.*, 2015). Unidirectional pores give better compressive strength when measured in an out-of-plane direction. Similarly, permeability is highest along the pore orientation as reported in the case of scaffolds produced by the freeze-drying technique. The orientation of the cells was measured in terms of the angles of the major axis of ellipsoids fitted within the volume of the cell with respect to the horizontal plane. This frequency distribution with respect to orientation angles is also shown in Fig. 6(c) whereas the mean and standard deviations are included in Table 1. The evaluation of these features reveals that there is a certain degree of preferential alignment in the 0–10 kGy samples, which decreases at higher doses.

**3.2.6. Pore and strut connectivity.** 3D imaging of microstructure using synchrotron-based X-ray micro-tomography allows quantification of pore and strut network connectivity using image analysis. This measurement can be of particular value for the characterization of transport properties of fluids within cellular structures (Xiong *et al.*, 2016; Berg *et al.*, 2016; Hormann *et al.*, 2016; Bernabé *et al.*, 2010, 2016). We have calculated the Euler number and 3D connectivity density for characterizing connectivity in porous microstructures of various irradiated PUF samples. The Euler number is a measure of the topology of porous media, expressing the multi-connectivity of a volume, and can be used to compare the way pores are interconnected. The Euler number is defined as  $\chi = N - C + H$ , where  $N$  is the number of isolated pores,  $C$  is the number of redundant connections within the pore space and  $H$  represents the number of completely enclosed cavities in 3D. Hence the Euler number is a measure of the connectivity which gives positive values for poorly connected structures where  $N > C$ . Connectivity density can be calculated by dividing the connectivity estimate of the Euler numbers by the volume of the sample. The 3D reconstruction enabled the visualization of pore inter-connectivity in the overall specimen. As shown in Table 2, it was observed from the trend of the negative value of the Euler number and 3D connectivity density that the connectivity increases with the initial lower dose of gamma irradiation up to 10 kGy due to cross linking in pores, and then decreases at higher doses due to chain scission.

**Table 2**  
Quantitative parameters related to the porosity and connectivity of the pore network.

	0 kGy	5 kGy	10 kGy	15 kGy	20 kGy
Total volume ( $\mu\text{m}^3$ )	$3.40 \times 10^{10}$	$1.31 \times 10^{10}$	$2.47 \times 10^{10}$	$1.42 \times 10^{10}$	$1.25 \times 10^{10}$
Polymer volume ( $\mu\text{m}^3$ )	$5.00 \times 10^9$	$2.36 \times 10^9$	$4.73 \times 10^9$	$2.41 \times 10^9$	$2.08 \times 10^9$
Pore volume ( $\mu\text{m}^3$ )	$2.9 \times 10^{10}$	$1.07 \times 10^{10}$	$1.99 \times 10^{10}$	$1.17 \times 10^{10}$	$1.04 \times 10^{10}$
Polymer volume fraction	0.147	0.180	0.191	0.170	0.166
Porous volume fraction	0.853	0.820	0.809	0.830	0.834
Total porosity	85.3%	82.0%	80.9%	83.0%	83.4%
Euler number	-52076	-53716	-68487	-47951	-30854
Connectivity density	95628	124044.75	142273.375	64400.25	40327.625
Degree of anisotropy	1.444	1.753	1.06	1.478	1.461
Fractal dimension	2.77	2.76	2.75	2.74	2.75

**3.2.7. Degree of anisotropy.** The degree of anisotropy is a measure of the 3D structural symmetry, which measures the presence, or absence, of preferential alignment of structures along a particular direction. Apart from the degree of connectivity or 3D connectivity density, the degree of anisotropy is a crucial determinant for the mechanical strength of cellular materials (Muljadi *et al.*, 2016; Ketcham & Ryan, 2004). The calculation of the degree of anisotropy uses the mean intercept length method in which a large number of vectors of the same length originating from a random point within the sample are drawn through the sample. When each vector hits a boundary between foreground and background, an intercept is counted for that vector. The mean intercept length on that vector is then the vector length divided by the number of boundary hits. A cloud of points is built up, where each point represents the vector times its mean intercept length. Fitting an ellipsoid to the point cloud, we construct a material anisotropy tensor, and subsequently Eigen decomposition results in Eigen values giving the lengths of the ellipsoid's axes and Eigen vectors giving the orientation of the axes (Doube *et al.*, 2010). The degree of anisotropy for different irradiated polyurethane samples is included in Table 2. Due to the initial irradiation of low dose and induced cross linking, the inhomogeneous shrinking leads to increased values of the degree of anisotropy for the 5 kGy sample, which is decreased reasonably in the 10 kGy samples, having good homogeneity of porous micro-structure, as can be seen in Fig. 2. A subsequent increase of dose leads to inhomogeneity of the porous microstructure and thus an increased value of the degree of anisotropy.

#### 4. Discussion

The chemistry of PUF makes use of poly addition reactions of organic isocyanate with compounds containing at least two active hydrogen atoms. The isocyanate group then reacts with the hydroxyl group of the polyol/diol to form the repeating urethane linkages (Engels *et al.*, 2013; Yusuf *et al.*, 2016). Absorption of high-energy radiation during  $\gamma$  irradiation causes excitation and ionization. These excited and ionized species are the initial chemical reactants for the degradation/cross-linking reactions of polymeric chains. The absorption of radiation forms free-radical sites at various bond segments, which include COOH,  $\text{NH}_2$ ,  $\text{C}=\text{C}$  *etc.* chemical bonds. Two

adjacent polymeric radicals, formed due to absorbed radiation energy, then join together to establish a cross-link. Formation of many such cross-links between the polymeric chains of the polyurethane leads to increased strain around the polymer molecule due to the absorbed radiation energy. Consequently, after a certain dose, the molecule may no longer withstand the increased strain, and absorption of radiation breaks down the backbone ( $-\text{C}-\text{C}-\text{NH}-\text{C}-$ ) of the polymeric chain

(Shintani & Nakamura, 1991; Shintani *et al.*, 1991). Upon irradiation, formation of cross-links, *i.e.* C–C covalent links between the long-chain molecules, or breakage of bonds between these molecules may dominate in a given polymer depending upon the bond energy of the polymer molecules and irradiation dose (Craven *et al.*, 2012). At macroscopic scales, these effects are seen in terms of modified molecular weight, release of hydrocarbons, production of residual radicals, and slight change in chemistry (Clough, 2001; Sui *et al.*, 2013; Labouriau *et al.*, 2015a). Several post-irradiation characterization methods have been utilized to understand the irradiation effects on various properties. For example, gel fraction for measuring the degree of network modifications, electron and optical microscopy for structure and rheology, differential scanning calorimetry for thermal analysis, electron spin resonance, IR and Raman spectroscopy for oxidation state, *etc.* have been used (Benouali *et al.*, 2005; Chien *et al.*, 2000; Labouriau *et al.*, 2015b). A moderate number of radiation-induced cross-links can either improve the mechanical property of cellular materials or make their response stiffer and brittle depending upon the density of the material (Craven *et al.*, 2012). Cross-linked materials may show improved mechanical properties such as more strength, better resistance to impact and stress cracking, improved creep resistance, and increased hardening, tensile strength, elongation at break (Clough, 2001). The transport properties are also seen to be changed in the form of changed heat capacity, modified heat deformation, thermal elongation (Chen *et al.*, 2015). Radiation-induced cross-linking, degradation and generation of free radicals also leads to several structural and morphological changes in polymer materials (Clough, 2001; Schaefer *et al.*, 2017; Consolati *et al.*, 2011; Fang *et al.*, 2017). These are observed in the form of modified porosity, physical density, surface morphology, cellular structures and network (Mrlik & Maadeed, 2016; Clough, 2001; Vachon & Gendron, 2003; Liu *et al.*, 2017; Hsiao *et al.*, 2012; Cardoso *et al.*, 2013). In particular, changes in cell structure and network are significant here as they play a significant role for the modification of mechanical and transport properties (Mrlik & Maadeed, 2016; Shintani & Nakamura, 1991; Shintani *et al.*, 1991; Labouriau *et al.*, 2015a).

In this study, we have for the first time utilized the synchrotron-based X-ray phase contrast micro-CT technique to evaluate gamma-irradiation-induced morphological varia-

tion in flame-retardant rigid PUF. Qualitative and quantitative comparisons show that these changes are not only prominent but they also systematically vary with irradiation dose as observed clearly in the form of cell size, porosity, wall thickness, pore shape and their spatial distribution. Quantitative comparison of pores size in terms of maximum opening and equivalent diameter clearly show that a low dose (0–10 kGy) of gamma irradiation reduces pore size and increases wall thickness. These effects are related to cross-linking between the neighbouring polymeric chains, which leads to increased wall thickness and shrinkage of cellular structure. At higher doses (10–20 kGy), the pore size increases again and the wall thickness decreases. The radiation dose also causes strain around the foam bubble, and therefore further exposure of gamma rays to higher doses leads to rupture at the cellular boundary connecting the bubble structure leading to increased pore size and decreased strut size. Similarly, porosity decreases and the physical density of material increases in the lower dose range, and the trend reverses at higher doses. The effect of radiation on these properties is nearly homogeneous throughout the sample. The connectivity and anisotropy of the porous network is also affected due to irradiation. Gamma-irradiation, however, does not impart any significant change in pore shape, strut shape and orientation. The effects of these micro-structural changes on compression behaviour of the PUF have been reported previously in the form of modifications in the compressibility of the material. Several models of structure property correlation have suggested a strong correlation between macroscopic mechanical behaviour of porous and cellular foam materials and porosity and other cellular microstructure properties (Veljović *et al.*, 2011; Maire *et al.*, 2003; Redenbach, 2009). In light of these models, the radiation-induced modulations in morphological parameters are reasonably translated to the variations in the mechanical properties of the foam. Although there is a strong correlation between irradiation-induced cellular microstructure variations and mechanical properties, the role of other factors such as changes in molecular weight, structural changes at other scales *etc.* contributing to the modified mechanical behaviour of PUF after irradiation cannot be ruled out. The exact nature of this correlation between cellular structural properties and the trend of mechanical compressibility needs a detailed study based on various empirical models and finite-element modelling based on *in situ* micro-tomography experiments, which is the subject of our future studies.

## 5. Conclusions

It is evident from the SR- $\mu$ CT-based qualitative and quantitative image analysis that the exposure to gamma radiation of PUF leads to significant and dose-dependent variations in its cellular microstructure. The smaller doses of gamma radiation in the range 0–10 kGy causes reduced pore size, increased strut size, decreased porosity, increased physical density, no significant change in pore shape and orientation, increased connectivity and decreased anisotropy. This is due to radiation-induced cross-linking in the low-dose range of gamma

irradiation. As the gamma dose is further increased to the 15–20 kGy range, chain scission effects start dominating over cross-linking, thus cellular structure is seen with increased pore size, decreased strut size, increased porosity, decreased physical density, no significant change in pore shape and orientation, decreased connectivity and increased anisotropy. Thus, it was shown that the gamma irradiation dose has strong effects on micro-structural properties of PUF due to chain scission and cross-linking effects in molecules. Future studies will aim to establish a well defined correlation between the microstructure of PUF and its mechanical properties under different loading conditions through empirical relations as well as finite-element modelling.

## References

- Agrawal, A. K., Singh, B., Kashyap, Y. S., Shukla, M., Sarkar, P. S. & Sinha, A. (2015). *J. Synchrotron Rad.* **22**, 1531–1539.
- Banhart, J. (2001). *Prog. Mater. Sci.* **46**, 559–632.
- Benouali, A., Froyen, L., Dillard, T., Forest, S. & N'guyen, F. (2005). *J. Mater. Sci.* **40**, 5801–5811.
- Berg, S., Rücker, M., Ott, H., Georgiadis, A., van der Linde, H., Enzmann, F., Kersten, M., Armstrong, R. T., de With, S., Becker, J. & Wiegmann, A. (2016). *Adv. Water Resour.* **90**, 24–35.
- Bernabé, Y., Li, M. & Mainault, A. (2010). *J. Geophys. Res.* **115**, B10203.
- Bernabé, Y., Li, M., Tang, Y.-B. & Evans, B. (2016). *OGST – Rev. IFP Energies Nouv.* **71**, 50.
- Bharti, A., Agrawal, A. K., Singh, B., Gautam, S. & Goyal, N. (2017). *J. Synchrotron Rad.* **24**, 1209–1217.
- Bharti, A., Bhardwaj, R., Agrawal, A. K., Goyal, N. & Gautam, S. (2016). *Sci. Rep.* **6**, 22394.
- Bhatt, C. U., Royer, J. R., Hwang, C. R. & Khan, S. A. (1999). *J. Polym. Sci. B Polym. Phys.* **37**, 1045–1056.
- Brabant, L., Vlassenbroeck, J., De Witte, Y., Cnudde, V., Boone, M. N., Dewanckele, J. & Van Hoorebeke, L. (2011). *Microsc. Microanal.* **17**, 252–263.
- Cardoso, E. C. L., Scagliusi, S. R., Parra, D. F. & Lugão, A. B. (2013). *Radiat. Phys. Chem.* **84**, 170–175.
- Chen, H., Liu, B., Huang, W. & Wu, W. (2015). *Polym. Degrad. Stabil.* **114**, 89–93.
- Chien, A., Maxwell, R., Chambers, D., Balazs, B. & LeMay, J. (2000). *Radiat. Phys. Chem.* **59**, 493–500.
- Choi, W. & Seo, K. (2010). *Nucl. Eng. Des.* **240**, 925–932.
- Choudhary, A., Pratihari, S. K., Agrawal, S. K. & Behera, A. K. (2017). *Adv. Eng. Mater.* **20**, 1700586.
- Clough, R. L. (2001). *Nucl. Instrum. Methods Phys. Res. B*, **185**, 8–33.
- Cnudde, V. & Boone, M. N. (2013). *Earth Sci. Rev.* **123**, 1–17.
- Consolati, G., Lotti, N., Mariani, M., Munari, A. & Quasso, F. (2011). *Polym. Degrad. Stabil.* **96**, 1297–1300.
- Craven, E., Hasanain, F. & Winters, M. (2012). *Radiat. Phys. Chem.* **81**, 1254–1258.
- Del Cui, G. D., Simmons, C. M., Icenhour, A. S. & Singh, D. (2006). *Radiolytic degradation of urethane foam used for encapsulation of contaminated components*. Report ORNL/TM-2006/15. Oak Ridge National Laboratory, Tennessee, USA (<https://info.ornl.gov/sites/publications/Files/Pub46695.pdf>).
- Diersch, R., Weiss, M. & Dreier, G. (1994). *Nucl. Eng. Des.* **150**, 341–348.
- Dolomanova, V., Rauhe, J. C. M., Jensen, L. R., Pyrz, R. & Timmons, A. B. (2011). *J. Cell. Plast.* **47**, 81–93.
- Doube, M., Klosowski, M. M., Arganda-Carreras, I., Cordelières, F. P., Dougherty, R. P., Jackson, J. S., Schmid, B., Hutchinson, J. R. & Shefelbine, S. J. (2010). *Bone*, **47**, 1076–1079.

- Eliceiri, K., Schneider, C. A., Rasband, W. S. & Eliceiri, K. W. (2012). *Nat. Methods*, **9**, 671–675.
- Engels, H., Pirkel, H., Albers, R., Albach, R. W., Krause, J., Hoffmann, A., Casselmann, H. & Dormish, J. (2013). *Angew. Chem. Int. Ed.* **52**, 9422–9441.
- Fang, H., Li, J., Chen, H., Liu, B., Huang, W., Liu, Y. & Wang, T. (2017). *Mech. Mater.* **105**, 148–156.
- Fatima, A., Kataria, S., Baghel, L., Guruprasad, K. N., Agrawal, A. K., Singh, B., Sarkar, P. S., Shripathi, T. & Kashyap, Y. (2017). *J. Synchrotron Rad.* **24**, 232–239.
- Gupta, C., Agarwal, A. K., Singh, B., Sarkar, P. S., Gadkari, S. C., Sinha, A., Srivastava, D. & Dey, G. K. (2017). *Mater. Sci. Eng. A*, **704**, 292–301.
- Hormann, K., Baranau, V., Hlushkou, D., Höltzel, A. & Tallarek, U. (2016). *New J. Chem.* **40**, 4187–4199.
- Hsiao, C., Liu, S., Wen-Neng Ueng, S. & Chan, E. (2012). *Polym. Degrad. Stabil.* **97**, 715–720.
- Jang, W., Kraynik, A. M. & Kyriakides, S. (2008). *Int. J. Solids Struct.* **45**, 1845–1875.
- Kaestner, A., Lehmann, E. & Stampanoni, M. (2008). *Adv. Water Resour.* **31**, 1174–1187.
- Kak, A. C., Slaney, M. & Wang, G. (2002). *Med. Phys.* **29**, 107.
- Kasperek, E., Zencker, U., Scheidemann, R., Völzke, H. & Müller, K. (2011). *Comput. Mater. Sci.* **50**, 1353–1358.
- Kenesei, P., Kádár, Cs., Rajkovits, Zs. & Lendvai, J. (2004). *Scr. Mater.* **50**, 295–300.
- Ketcham, R. A. & Ryan, T. M. (2004). *J. Microsc.* **213**, 158–171.
- Kim, D., Seo, K., Lee, J., Bang, K., Cho, C., Lee, S. J. & Baeg, C. Y. (2007). *Ann. Nucl. Energy*, **34**, 871–882.
- Kinney, J. H. & Nichols, M. C. (1992). *Annu. Rev. Mater. Sci.* **22**, 121–152.
- Labouriau, A., Cady, C., Gill, J., Stull, J., Ortiz-Acosta, D., Henderson, K., Hartung, V., Quintana, A. & Celina, M. (2015b). *Polym. Degrad. Stabil.* **116**, 62–74.
- Labouriau, A., Cady, C., Gill, J., Taylor, D., Zocco, A., Stull, J., Henderson, K. & Wroblewski, D. (2015a). *Polym. Degrad. Stabil.* **117**, 75–83.
- Limaye, A. (2012). *Proc. SPIE*, **8506**, 85060X.
- Liu, B., Wang, P., Ao, Y., Zhao, Y., An, Y., Chen, H. & Huang, W. (2017). *Radiat. Phys. Chem.* **133**, 31–36.
- Maire, E., Fazekas, A., Salvo, L., Dendievel, R., Youssef, S., Cloetens, P. & Michel, J. (2003). *Compos. Sci. Technol.* **63**, 2431–2443.
- Mane, J. V., Chavan, V. M. & Patel, R. J. (2017). *Procedia Eng.* **173**, 718–725.
- Marenzana, M., Hagen, C. K., Borges, P. D. N., Endrizzi, M., Szafranec, M. B., Vincent, T. L., Rigon, L., Arfelli, F., Menk, R. & Olivo, A. (2014). *Proc. R. Soc. A*, **372**, 20130127.
- Moreno-Atanasio, R., Williams, R. A. & Jia, X. (2010). *Particuology*, **8**, 81–99.
- Mrlík, M. & Al Ali Al Maadeed, M. (2016). *Polym. Degrad. Stabil.* **133**, 234–242.
- Muljadi, B. P., Blunt, M. J., Raeini, A. Q. & Bijeljic, B. (2016). *Adv. Water Resour.* **95**, 329–340.
- Palacio, A. (2017). *Energy Procedia*, **127**, 398–406.
- Pfeiffer, P. A. & Kennedy, J. M. (1989). *Nucl. Eng. Des.* **114**, 33–52.
- Redenbach, C. (2009). *Comput. Mater. Sci.* **44**, 1397–1407.
- Roberts, A. P. & Knackstedt, M. A. (1995). *J. Mater. Sci. Lett.* **14**, 1357–1359.
- Saadatfar, M., Arns, C. H., Knackstedt, M. A. & Senden, T. (2005). *Colloids Surf. A Physicochem. Eng. Asp.* **263**, 284–289.
- Saadatfar, M., Knackstedt, M. A., Arns, C. H., Sakellariou, A., Senden, T. J., Sheppard, A. P., Sok, R. M., Steininger, H. & Schrof, W. (2004). *Physica A*, **339**, 131–136.
- Saliba, R., Mourao, R. P., Quintana, F., Novara, O. & Silva, L. L. (2011). *Packag. Transp. Storage Secur. Radioact. Mater.* **22**, 172–178.
- Sanyal, D., Goyal, P., Verma, V. & Chakraborty, A. (2011). *Nucl. Eng. Des.* **241**, 3178–3189.
- Schaefer, C. E., Kupwade-Patil, K., Ortega, M., Soriano, C., Büyükköztürk, O., White, A. E. & Short, M. P. (2017). *Waste Manag.* **71**, 426–439.
- Seuba, J., Deville, S., Guizard, C. & Stevenson, A. J. (2016). *Sci. Rep.* **6**, 24326.
- Sharma, K., Pawaskar, D. N., Guha, A. & Singh, R. K. (2014). *Nucl. Eng. Des.* **273**, 190–201.
- Sheppard, A. P., Sok, R. M. & Averdunk, H. (2004). *Physica A*, **339**, 145–151.
- Shintani, H., Kikuchi, H. & Nakamura, A. (1991). *Polym. Degrad. Stabil.* **32**, 17–30.
- Shintani, H. & Nakamura, A. (1991). *Polym. Degrad. Stabil.* **32**, 191–208.
- Sui, H. L., Liu, X. Y., Zhong, F. C., Li, X. Y., Wang, L. & Ju, X. (2013). *Nucl. Instrum. Methods Phys. Res. B*, **307**, 570–574.
- Thirumal, M., Khastgir, D., Nando, G. B., Naik, Y. P. & Singha, N. K. (2010). *Polym. Degrad. Stabil.* **95**, 1138–1145.
- Thirumal, M., Khastgir, D., Singha, N. K., Manjunath, B. S. & Naik, Y. P. (2009). *J. Macromol. Sci. Part A*, **46**, 704–712.
- Vachon, C. & Gendron, R. (2003). *Radiat. Phys. Chem.* **66**, 415–425.
- Veljović, D., Jančić-Hajneman, R., Balać, I., Jokić, B., Putić, S., Petrović, R. & Janačković, D. (2011). *Ceram. Int.* **37**, 471–479.
- Xiong, Q., Baychev, T. G. & Jivkov, A. P. (2016). *J. Contam. Hydrol.* **192**, 101–117.
- Yusuf, A. K., Mamza, P. A. P., Ahmed, A. S. & Agunwa, U. (2016). *Intl J. Sci. Res. Publ.* **6**, 548–556.
- Zeng, T., Dong, X., Mao, C., Zhou, Z. & Yang, H. (2007). *J. Eur. Ceram. Soc.* **27**, 2025–2029.
- Zhou, S. A. & Brahme, A. (2008). *Phys. Med.* **24**, 129–148.